PHASE TOMOGRAPHY IN NEUTRON INTERFEROMETRY

M. Zawisky[1], U. Bonse[2], F. Dubus[1], R. Loidl[1,3], Z. Hradil[4], J. Rehacek[4]
[1] Atominstitute of the Austrian Universities, Vienna, Austria; [2] University of Dortmund, Dortmund, Germany; [3] Institute Laue Langevin, Grenoble, France; [4] Palacky University, Olomouc, Czech Republic;

Abstract: Perfect crystal neutron interferometry permits the simultaneous investigation of different interactions, like absorption, small angle scattering, and forward scattering. The coherent forward scattering of neutrons in materials or magnetic fields generates phase shifts, which can be detected with high sensitivity. The tomographic reconstruction of phase projections is similar to that of intensity projections in transmission tomography, but due to the larger fluctuation of count numbers and phases, an optimized maximum likelihood algorithm has to be engaged. We present first experimental results, the analysis of isotope mixtures, and the investigation of a metal alloy; both materials are nearly transparent to thermal neutrons. The neutron phase tomography proves its strength in extreme applications where other methods fail, e.g., the complete 3D analysis of non or weak absorbing substances and isotope distributions, the sensitive detection of liquids, residues and corrosion in metals, and the investigation of magnetic domains in bulk materials.

Introduction: The PCT (*Phase Contrast Tomography*) imaging technique was first invented in x-ray tomography [1,2], and has then successfully been transferred to neutron interferometry [3]. The perfect crystal interferometer is a very sensitive device for the detection of scattering effects in the sample, and it allows distinguishing between different interactions, like absorption, small angle scattering (SAS), and coherent forward scattering. The coherent scattering in the sample yields detectable phase differences between the two interfering beams, the object beam through the sample, and the reference beam [4]. While x-ray PCT is sensitive to the electron density and the atomic number Z, the neutron (nPCT) technique depends solely on nuclear and magnetic interaction. Therefore x-ray and neutron PCT are complementary techniques, always sensing different material features. The sensitivity of the new nPCT method has to be compared with attenuation tomography. It is found that the nPCT sensitivity is three orders of magnitude higher than that of conventional CT for most isotope mixtures. Interferometric imaging is experimentally more demanding because it requires a strong neutron source, temperature stabilization and vibration shielding. But nPCT could be of particular interest in extreme applications, like the investigation of substances with very weak absorption, the visualization of isotopic distributions with high sensitivity, and the analysis of magnetic domains in bulk materials.

Theory: The principle of interferometric imaging is sketched in Fig. 1. The entrance beam, monochromatic neutrons of wavelength $\lambda \cong 0.192$ nm, is coherently split into the reference beam and the object beam at the first crystal lamella. When the object beam passes the sample it experiences phase shifts which then generate detectable phase differences between the object and reference rays. The accumulated phase shifts Φ through the sample create a phase-sensitive intensity pattern at the interferometer output. The interference pattern is modulated by an auxiliary phase shifter, which generates a series of controlled phase differences Δ_j between object and reference beams. This measurement procedure allows the determination of Φ_{xz} for every individual pencil beam of cross section dxdz in the corresponding detector pixel at position (x,z).

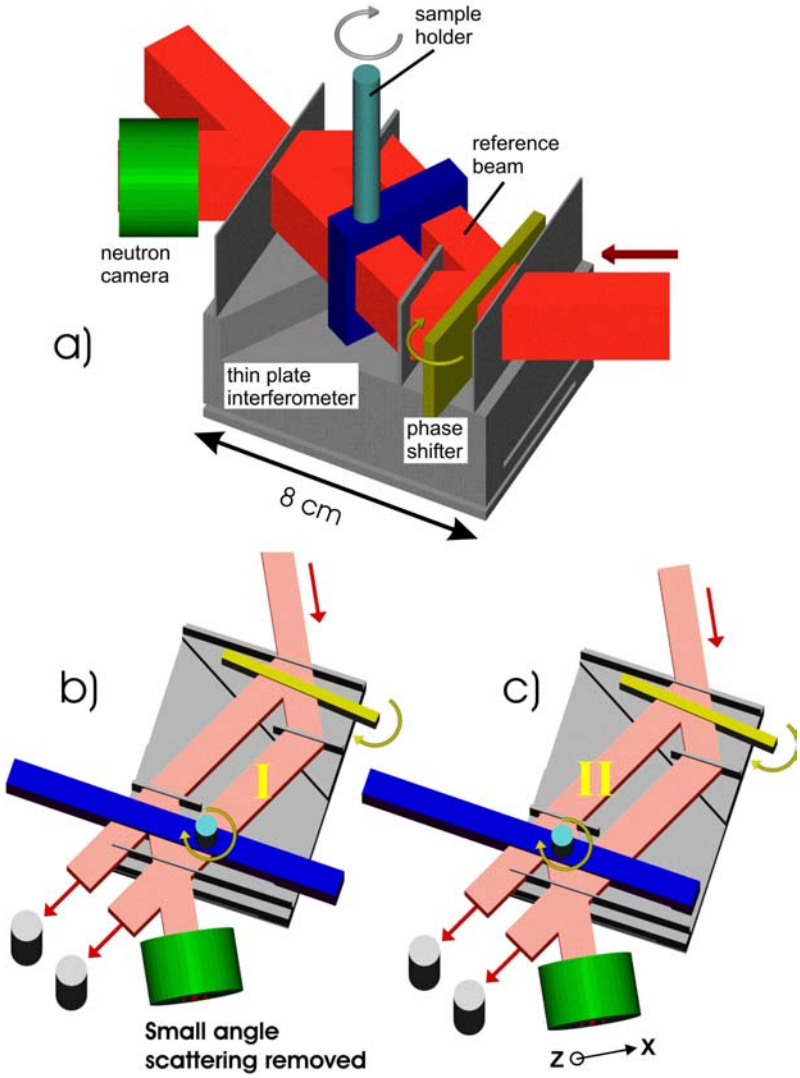

The phase-modulated count numbers in the detector pixels (x,z) follow a harmonic oscillation:

$$I_{xz,j} = \frac{\bar{I}_{xz,0}(1+t_{xz})}{2}\left(1+V_{xz}\cos(\Delta_j+\Phi_{xz})\right) \quad (1)$$

$\bar{I}_{xz,0}$ is the mean count number in beam I,II if absorption is negligible. The absorption in the sample is described by the transmission probability t_{xz}. If the sample is placed in beam I then the transmission is reduced by scattering (cross section σ_s), small angle scattering (σ_{sas}), and absorption (σ_a):

$$t \cong \exp\left[-\sum_i N_i(\sigma_s+\sigma_{sas}+\sigma_a)_i\, d\right] \quad (2)$$

N_i denotes the nuclear density of the different isotopes in the sample, and d the thickness. Small angle scattered neutrons are filtered out by the last interferometer lamella in Fig.1b. If the sample is placed in beam II then SAS contributes to the output intensity and the transmission will be higher. The comparison of the two configurations yields structural information beyond the spatial detector resolution. SAS due to refraction on the edges is also useful for contrast enhancement of the sample shape [3,5].

The measurement of transmission t_{xz} enables a conventional CT analysis of the sample. Here, the use of perfect crystal devices has the advantage that beam hardening artefacts are completely suppressed [6].

The visibility V_{xz} of interference fringes depends on the quality of the interferometer setup, but V_{xz} is also affected by dephasing in the specimen. Strong dephasing and low visibilities indicate a large gradient of scattering densities $\Delta(N_i b_{ci})$. Although dephasing reduces the visibility and therefore the phase sensitivity, it contains additional information about micro-inhomogeneities below the pixel resolution.

The most important quantity in interferometric imaging is the phase shift in the sample:

$$\Phi_{xz} = -\lambda \int_{ray} \sum_{i} (N_{xz} b_c)_i \, ds \qquad (3)$$

The accumulated phase shift along a pencil beam through the sample depends on the wavelength λ, the nuclear densities N_i of the different isotopes i, and the coherent scattering length b_{ci} , which is accurately known for most isotopes [7]. The phase shift is negative for repulsive potentials, but there exist some isotopes with negative b_c characterizing weak attractive interactions. The enhanced sensitivity of perfect crystal nPCT can be expressed by a gain factor ($\lambda V b_c/\sigma$). It turns out that the sensitivity in detecting small density variations ΔN_i is 10^3 times higher in nPCT than in conventional transmission tomography for most isotopes. But the achievable phase resolution is limited by the statistical phase uncertainty [8]:

$$\Delta\Phi_{xz} \cong \frac{\sqrt{2}}{\sqrt{I_{xz}}\, V_{xz}} \qquad (4)$$

From Eq. (4) follows that the sensitivity is restricted by the total count number $I_{xz} = \sum_j I_{xz,j}$ in the detector pixel, and the visibilities ($0 < V_{xz} < 1$). Given typical experimental parameters ($I_{xz} \approx$ 30-800 n, $V_{xz} \approx 0.5$) the estimated phase resolution is 5° - 30°, and the corresponding sensitivity $\Delta(Nb_c)/(Nb_c) \approx 10^{-2}$. Large scattering length differences, e.g., Δb_c = 20.82 fm between light and heavy water, enhance the detection sensitivity for ΔN. The spatial resolution is mainly limited by the beam divergence and the detector to sample distance. In the present experiment we achieve a resolution of 50 μm in horizontal and vertical direction, which corresponds to the pixel resolution of the scintillation detector. A further increase of spatial resolution is feasible with a better beam collimation, but at the expense of utilizable intensity. Stronger monochromatic neutron beams and advanced digital neutron detectors with higher resolution and efficiency are needed for exploiting the full nPCT potential.

Results: To demonstrate the superiority of nPCT compared with conventional transmission tomography we have chosen weakly absorbing substances, like aluminium with slightly varied elemental composition, sulphur isotopes, and mixtures of light and heavy water. In these samples the neutron absorption is negligible. The first specimen is shown in Fig. 2. It consists of several aluminium parts, including an Al-rod with a coaxial Al-screw in the object beam. The screw has a

slightly different chemical composition than the surrounding aluminium rod and block (see Table 1). The goal was the visualization and quantitative analysis of the embedded screw with its 2% lower scattering density. The sample is a metric screw with 6 mm outer diameter, 1 mm nominal pitch, and a length of 21 mm. The Al-rod, which encloses the screw, has a diameter of 7 mm, and the Al-block a thickness of 8 mm.

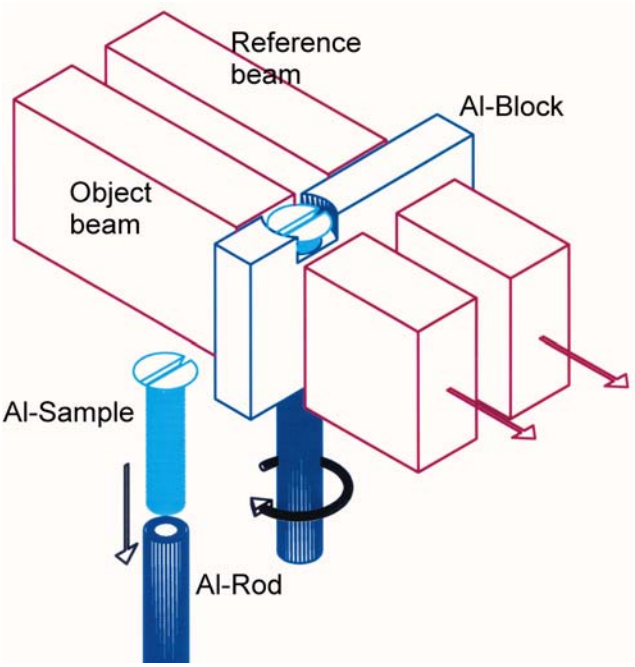

Table 1 Elemental composition of the aluminium parts

	Element	A[g]	b_c[fm]	Sample $wt\%$	Rod, Block $wt\%$	Sample $Nb_c \times 10^{-7}$ cm^{-2}	Rod, Block $Nb_c \times 10^{-7}$ cm^{-2}
	Al	26.98	3.449	92.01	92.52	1914.54	1923.16
N	Mg	24.31	5.375	3.09	5.02	110.5	181.08
	Si	28.09	4.15	0.43	0.88	10.68	21.37
	Mn	54.94	-3.73	0.5	0.29	-5.52	-3.208
	Fe	55.85	9.45	0.3	0.15	8.22	4.158
SR	Cu	63.55	7.718	2.66	0.97	52.56	19.14
	Zn	65.41	5.68	0.14	0.04	1.977	0.562
	Pb	207.2	9.405	0.87	0.12	6.42	0.884
						Total: 2099.38	**Total: 2147.15**

The largest difference in the scattering density stems from the lower Mg content in the screw, therefore the phase shifts are mainly generated by the different magnesium content. The same analysis performed with x-rays would yield the copper variation as primary result. This emphasizes the complementarity between nPCT and xPCT. Fig. 3 shows the tomographic reconstruction of the screw using a filtered-backprojection algorithm from 30 projections.

Our first result leads us to believe that in the present nPCT arrangement the detection limit of scattering length variations is well below 2%.

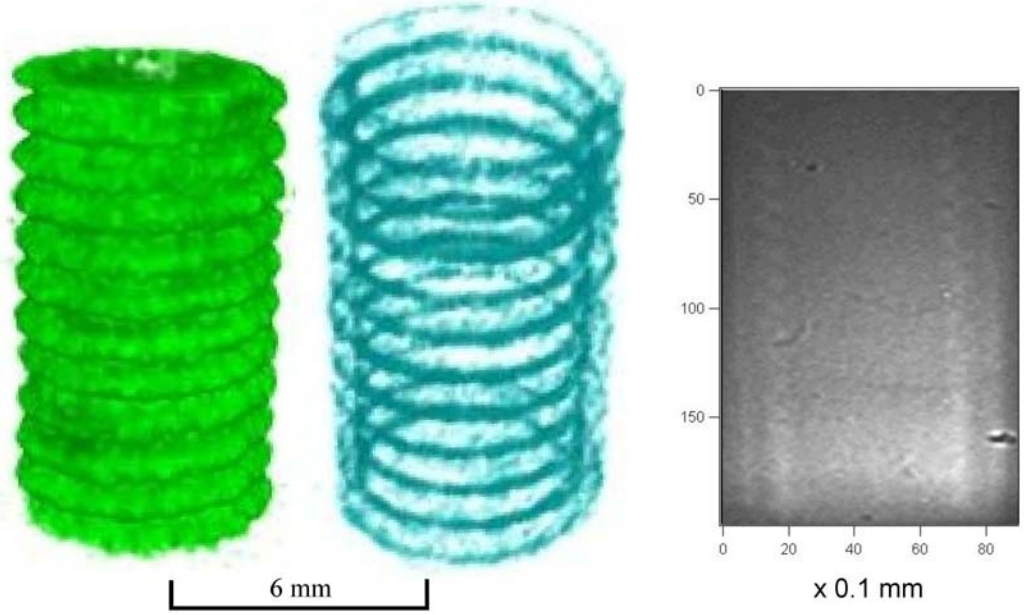

Fig. 3 Left: Tomographic reconstruction of the aluminium screw from phase shifts in the sample.

Middle: The 100 μm air gap in the thread creates a strong phase difference relative to the Al-block in the reference beam.

Right: Transmission image; the bulk of the screw is not visible because the neutron absorption in aluminium is negligible; the thread of the screw can be guessed due to refraction on the edges.

The second specimen consists of different sulphur isotope mixtures, pressed in a central bore hole as sketched in Fig. 4. We used the same aluminium sample holder and aluminium block as shown above. Again the sulphur isotopes are invisible in the transmission image because of their small absorption cross sections. The intensity modulations shown in Fig. 4 are created by interference between the object and the reference beams at three reference phases $\Delta_j = 0°, 120°, 240°$. Moreover, the three images in the top row of Fig. 4 are purely phase contrast images because small angle scattering is removed with the sample in beam I. Three phase-modulated images are sufficient for the derivation of the unknown phase shifts Φ_{xz}. For the tomographic analysis we used again 30 phase projections, i.e., 30 × 3 intensity images. Only in the ($S_{element}$+Al_2O_3) region we found strong small angle scattering, which creates a bright offset with the sample in beam II. This is an example how different scattering effects become distinguishable in perfect crystal interferometry.

At the top of the rotatable sample holder two additional bore holes have been filled with isotope mixtures of light and heavy water. The difference in the H_2O mass fraction is below 10^{-2} but the phase sensitivity is sufficient to resolve such small variations. To quantify the phase sensitivity it is necessary to calculate the scattering densities of the different isotope mixtures. Table 2 compares calculated and measured phase differences between the H_2O/D_2O mixtures, and between two sulphur mixtures.

This specimen was primarily designed as gauge for exploiting the nPCT resolution, and for developing an optimized maximum likelihood reconstruction technique.

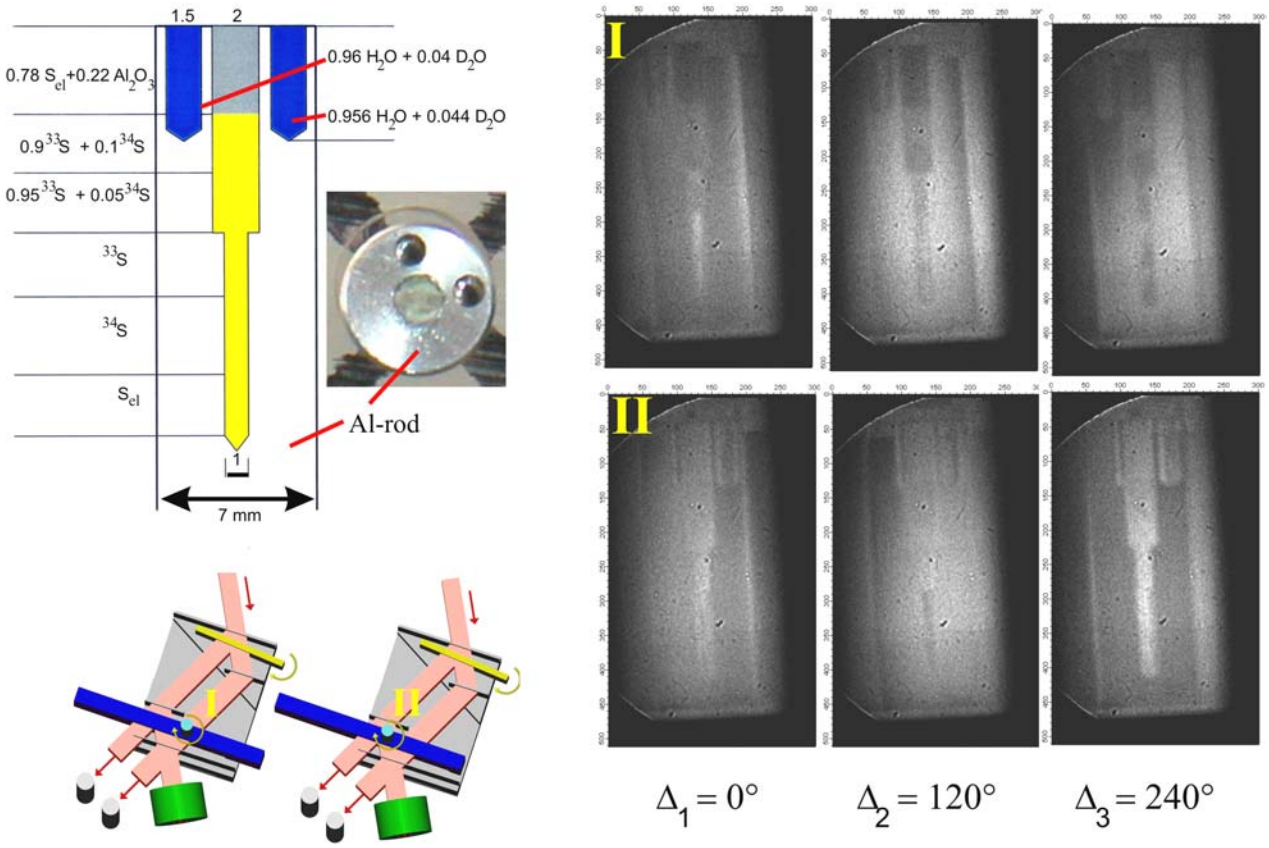

Fig. 4 Isotope gauge for the derivation of the present nPCT resolution.

Table 2 Phase differences in the isotope mixtures

Isotope mixture	Scattering density (Nb_c)	Diameter of the bore hole (d)	Expected phase difference	Measured phase difference
0.956 H_2O + 0.044 D_2O 0.960 H_2O + 0.040 D_2O	-2.55×10^9 cm^{-2} -2.82×10^9 cm^{-2}	1.5 mm 1.5 mm	45° (max)	36° ± 9°
0.95 ^{33}S + 0.05 ^{34}S 0.90 ^{33}S + 0.10 ^{34}S	1.725×10^{10} cm^{-2} 1.703×10^{10} cm^{-2}	2 mm 2 mm	48° (max)	45° ± 8°

Maximum likelihood reconstruction: Compared to the reconstruction presented in Fig. 3, the full tomographic reconstruction of the isotope gauge shown in Fig. 4 is considerably more involved due to smaller counted numbers of neutrons and large total phase shifts up to ~1000°

introduced by the isotopes filling the central cylinder. The resulting phase jumps are difficult to correct because of the large statistical noise and the limited detector resolution. For that reason, it is necessary to replace the standard filtered-backprojection algorithm by the more sophisticated maximum-likelihood (ML) method. The log-likelihood of the given distribution of the scattering density reads,

$$\log L = \sum_{p,j} n_{jp} \log\left[\bar{I}_p\left(1 + V_p \cos\left(\Delta_{jp} + \Phi_p\right)\right)\right] - I_{tot} M \tag{5}$$

where $\bar{I}_p$, V_p, and Φ_p are mean count numbers, visibility and total accumulated phase corresponding to pth projection, respectively, Δ_{jp} are the auxiliary phase shifts at the M phase shifter positions, n_{jp} are registered counts, and I_{tot} is the sum over all projections $\bar{I}_p$. For the purpose of reconstruction we represent the total phase by a discrete sum $\Phi_p = \sum_k c_{pk} (Nb_c)_k$, where the coefficients c_{pk} quantify the overlap of pth projection and kth cell of the reconstruction mesh. In deriving (5) we assumed that the statistics of the detected counts was Poissonian. The likelihood (5) can be maximized by an iterative procedure of the expectation-maximization type. A nice feature of ML approach is that together with phases, the visibilities corresponding to individual projections are estimated too. Since the likelihood (5) is a weighted sum of these individual contributions, the data leading to higher visibilities have larger influence on the result of the reconstruction. This means that unlike the standard filtered-backprojection, our ML procedure "trusts'' the data with larger phase sensitivity more than data containing little or no phase information. The details of the ML-PCT method will be presented elsewhere [9]. Let us just point out that this method is capable of handling very noisy data and, to a certain extent also data exhibiting phase jumps.

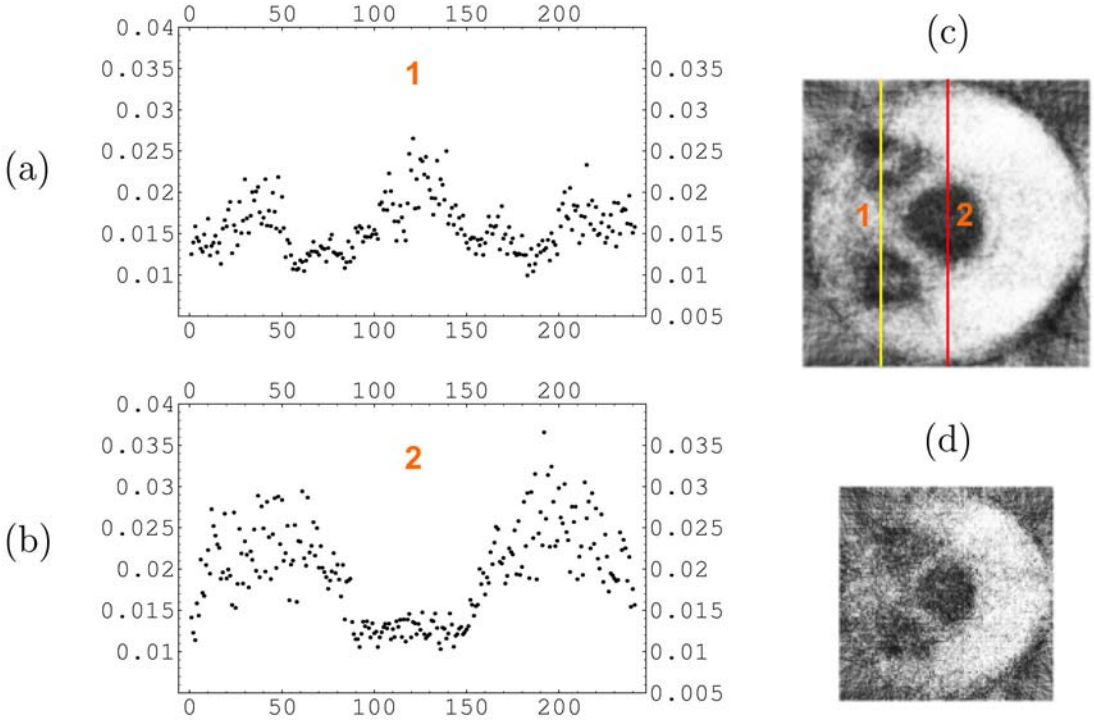

Fig. 5 ML phase contrast tomography of a cut through the upper part of the isotope gauge. Reconstructed scattering densities (in arbitrary units) are shown (a) along a line connecting the water cylinders with
$(\Delta Nb_c)/ Nb_c \sim 10\%$ between the two water mixtures, as expected from table 2; (b) along a line through the central sulphur mixture, where the scattering density is considerably lower. (c) 2D visualisation of the whole slice. In (a), (b), and (c) data were averaged over 10 slices. Panel (d) shows the reconstruction of a single slice of 50 μm thickness in the same region; the reconstructed area covers 160×160 detector pixels or 8×8 mm^2.

The developed technique has been applied to the nPCT measurement of the isotope gauge shown in Fig.4. For the reconstruction, we chose a cut through the upper part of the cylinder, where sample's geometry is not trivial, despite both intensity and visibility drop almost down to zero in this region. This makes the experimental data a challenge for any reconstruction method. Our results are summarized in Figure 5. As a first trial, we averaged data over 10 adjacent slices to increase the signal-to-noise ratio. Note that no binning in the transversal direction was done. Thus we could exploit the full 50 μm resolution of the detector. As can be seen in Fig. 5c, the water filled cylinders as well as the central cylinder filled with a mixture of sulphur element and aluminium oxide are revealed in the reconstructed image. Given the extreme experimental conditions (small intensities, bad visiblility, only 30 measured projections), and given that data without any prior filtering were used, the result is surprisingly good. Panels 5a and 5b depict two particular line profiles of the scattering density. Profile 5a suggests that both water mixtures have only slight differences in the scattering cross sections, which is consistent with the analysis of the previous section. As a second step, we applied the same routine to a single slice, see Fig. 5d. Though noise is significantly increased, it is still possible to distinguish the geometry of the isotope distribution. We would like to emphasis that in this case, typical counts were around 30 particles detected per pixel. Yet the ML reconstruction was able to give a meaningful result.

Conclusions: We introduced a new tomographic technique, the phase contrast tomography with neutron beams, and we demonstrated the high sensitivity of nPCT in neutron interferometry. The nPCT technique proves its strength where other methods fail, e.g. in the sensitive analysis of isotopic density variations. The sensitivity of nPCT is mainly limited by the low counting numbers, but state-of-the-art reconstruction algorithms can partly compensate the statistical fluctuations. Presently, we achieve a sensitivity of about 1% in the analysis of density variations of isotope mixtures. A spatial resolution up to 50 μm has been utilized in our measurements. As future nPCT applications we consider the sensitive 3D analysis of weak absorbing substances and isotope distributions, residues and corrosion in metals, and the investigation of magnetic domains in bulk materials [10].

Acknowledgement: This work was financially supported by the EURATOM-ÖAW, UT4-Underlying Technology project, and grant No. LN00A015 of the Czech Ministry of Education.

References:

[1] A. Momose, Nucl. Instr. and Meth. A352 (1995) 622.
[2] F. Beckmann, U. Bonse, F. Busch, O. Günnewig, J. Comput. Assist. Tomogr. 21(4) (1997) 539.
[3] F. Dubus, U. Bonse, M. Zawisky, M. Baron, R. Loidl, IEEE Transactions of Nuclear Science, in print
[4] H. Rauch, S.A. Werner, Neutron Interferometry, Oxford University Press (2000).
[5] M. Hainbuchner, M. Villa, G. Kroupa, G. Bruckner, M. Baron, H. Amenitsch, E. Seidl, H. Rauch,
J. Appl. Cryst. 33 (2000) 851.

[6] F. Dubus, U. Bonse, Th. Biermann, M. Baron, F. Beckmann, M. Zawisky, Proc. of SPIE Vol. 4503 (2002) 359.
[7] V.F. Sears, Neutron News 3, No. 3 (1992) 26.
[8] H. Rauch, J. Summhammer, M. Zawisky, E. Jericha, Phys. Rev. A42 (1990) 3726.
[9] J. Rehacek, Z. Hradil, M. Zawisky, "Phase-contrast tomography with low intensity beams,'' to be published.
[10] G. Badurek, R.J. Buchelt, H. Leeb, R. Szeywerth, Physica B335 (2003) 114.